Development of $La_xCa_{1-x}MnO_3$ materials for Bezaktiv Blue removal in aqueous media

É. V. Nascimento, A. M. Garrido Pedrosa and M. J. B. Souza

ABSTRACT

In this work, mixed oxides of $La_xCa_{1-x}MnO_3$ perovskite type (x = 0, 0.5 and 1.0) were synthesized through modified proteic method using collagen and calcination process at 700 °C/2 h in order to remove the commercial textile dye Bezaktiv Blue S-MAX from water. Oxides were characterized using X-ray diffraction (XRD), Fourier transform infrared spectroscopy (FTIR), N_2 physisorption, scanning electron microscopy (SEM) and point of zero charge (PZC) techniques while the dye only by the first two techniques. The XRD showed that perovskite monophase was obtained for x = 0.5 and 1.0. However, for x = 0, the low crystalline perovskite phase was obtained in the midst of precursor oxides. FTIR showed the adsorption process did not damage the adsorbents structure. The successful obtained materials have meso and macroporous with slit or cavity shape, rough surface and particles with varying sizes. The pseudo-second-order model was the one that best fit the kinetic data. The process must occur through electrostatic surface interactions between the adsorbent surface and the dye molecule. For the equilibrium study, Langmuir isotherm is the most suitable when using $LaMnO_3$ adsorbent, while Freundlich isotherm was better suited when used the other two materials. The adsorbents were termally regenerated and reused five times. The best performance was exhibited by $LaMnO_3$.

Key words | adsorption, Bezaktiv Blue, modified proteic method, perovskite oxide, regeneration, reuse

HIGHLIGHTS

- Successful preparation of $La_xCa_{1-x}MnO_3$ (x = 0.5 and 1.0) materials using low cost method.
- Effective removal of Bezaktiv Blue dye using $La_xCa_{1-x}MnO_3$.
- The $LaMnO_3$ maintained your adsorptive capacity throughout regeneration cycles.
- The $La_{0.5}Ca_{0.5}MnO_3$ became a catalyst after the second regeneration and the $CaMnO_3$ had its structure consolidated throughout regeneration cycles.
- The materials pores contributed to adsorption process.

É. V. Nascimento
M. J. B. Souza
Graduate program in Chemical Engineering,
Federal University of Sergipe,
Av. Marechal Rondon, Rosa Elze, São Cristóvão, SE 49100-000,
Brazil

A. M. Garrido Pedrosa (corresponding author)
Department of Chemistry,
Federal University of Sergipe,
Av. Marechal Rondon, Rosa Elze, São Cristóvão, SE 49100-000,
Brazil
E-mail: *annemgp@ufs.br*

doi: 10.2166/wst.2021.174

GRAPHICAL ABSTRACT

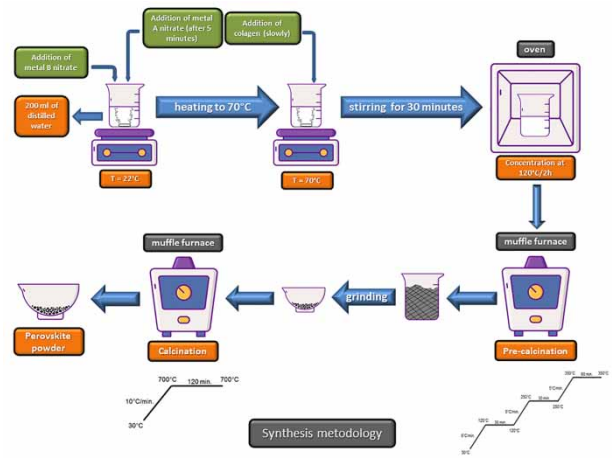

INTRODUCTION

Recently, nanomaterials used as synthetic adsorbents have attracted a lot of interest from researchers because their distinct properties such as electronic conduction, considerable specific surface area, high surface area/volume ratio (compared to microporous adsorbents), highly active sites presence, small amount of mass used and the ability to modify its surface properties. In addition, the ease of synthesis at low cost and the considerably greater adsorptive capacity are also significant advantages. Since nanomaterials exhibit unique properties, research on them is gradually becoming more popular and meaningful (Chen 2011; Tavakkoli & Yazdanbakhsh 2013; Rakass *et al.* 2018).

In general, scientific research on new adsorbents can be divided into two lines. In the first, it seeks to take advantage of agro-industrial waste or abundant raw materials available in nature. In the second, it looks to synthesize new adsorbents or develop the existing ones. In the first research line, adsorbents have low cost to obtain, as they are cheap by their very nature and not require elaborate processing before being used. However, the adsorptive capacities presented are not always high, requiring large adsorbent masses for the effluent treatment. In addition, these adsorbents cannot be recovered due to their own structural condition, being loaded with adsorbate and thus generating another waste, which disposal can not be done randomly. Another negative point is the fact these materials have a varied composition, requiring a homogenization pretreatment before being used.

On the other hand, the second research line involves synthesis of adsorbents that are homogeneous, have a well-defined composition and considerable adsorptive capacity and can be regenerated without suffering structural damage, thus maintaining their adsorptive capacity over several adsorption cycles, can be reused several times. Because they are carefully synthesized, these materials may even have other properties of industrial interest, such as selectivity over an effluent composed of various substances.

Within second research line appear the perovskite type mixed oxides, a new class of adsorbent materials with ABO_3 structure, A being generally an alkali metal, alkaline earth or rare earth and B a metal of external transition block (Tanaka & Misono 2001; Zhu *et al.* 2014; Attfield *et al.* 2015). This materials class has been subject of numerous studies in recent decades due to its easy obtaining and because they are applied in the industrial, environmental and technological sectors. Its outstanding properties are catalytic, redox, adsorptive, electrical, optical, magnetic, ferroelectric and superconductivity, in addition to generally shown of good mechanical, thermal and hydrothermal stability. All of them depends on composition, oxide structure and synthesis method (Peña & Fierro 2001; Hardin *et al.* 2014; Zhu *et al.* 2014; Fernandes *et al.* 2020; Lemos *et al.* 2020). Perovskite type oxides are generally synthesized by means of synthesis methodologies that employ high temperatures and calcination times, besides many chemical reactants and steps. In recent years, the modified proteic method has stood out for being an alternative, low cost and less aggressive to the environment to produce those materials. In addition, the temperatures typically required

to obtain the crystalline phase are generally lower (Santos *et al.* 2018; Ribeiro 2019; Souza 2019; Fernandes *et al.* 2020; Lemos *et al.* 2020; Nascimento *et al.* 2020).

These oxides constitute a very versatile compounds class, since their properties can be easily modified/manipulated or by changing the chemical composition, through the introduction of doping elements (cations partial replacement), or by modifications in the synthesis methods (Tummino *et al.* 2017). When the La^{3+} ions of $LaMO_3$ are replaced by alkaline earth ions, like Ca^{2+}, forming $La_{1-x}Ca_xMO_{3-\delta}$, a positive charge can be generated. If the M cations have different oxidation states, the charge neutrality can be maintained through the oxygen vacancies formation and changes in the other cations valence states. Because of this, these mixed oxides can have electrical conductivity, catalytic activity, mechanical properties and colossal magnetoresistance (Tavakkoli *et al.* 2014). In addition, A-site doping with calcium is expected to maintain/improve the lanthanum manganite adsorptive properties and decrease obtaining cost, since the calcium reagent is cheaper than lanthanum reagent.

Therefore, the objective of this work is to synthesize the oxides with $La_xCa_{1-x}MnO_3$ ($x = 0$, 0.5 and 1.0) perovskite structure through the modified proteic method, characterize them using X-ray diffractometry (XRD), Fourier transform infrared spectroscopy (FTIR), N_2 physisorption, scanning electron microscopy (SEM) and point of zero charge (PZC) determination techniques and evaluate them in removal of Bezaktiv Blue S-MAX (BB) dye dissolved in aqueous solution. Finally, a study was carried out on the regenerability and reuse of obtained adsorbents, evaluating the adsorptive capacity behavior throughout the adsorption–regeneration cycles. There is very little information in the literature about BB. Its safety data sheet (Bestchem 2020) only indicates that dye is reactive, bifunctional, chemically stable, metal-free and highly soluble in water.

METHODS

Synthesis of $La_{1-x}Ca_xMnO_3$

The $La_{1-x}Ca_xMnO_3$ ($x = 0$, 0.5 and 1.0) materials were synthesized through modified proteic method similar to that reported by Santos *et al.* (2018), however, with some modifications. The modifications in the synthesis methodology were proposed in order to reduce the temperature and time for calcination of the materials to obtain the desired phase. The experimental parameters for the synthesis (temperature, time, and mass, among others) were defined based on previous studies (Santos *et al.* 2018; Ribeiro 2019; Souza 2019). Stoichiometric calculations have been made for obtain 4 g of each final material after calcinations. Initially, manganese nitrate ($Mn(NO_3)_2.4H_2O$ – Neon, 98.8%) was dissolved in 200 mL of distilled water at room temperature (23 °C), under stirring, for 5 min. Then, lanthanum nitrate ($La(NO_3)_3.6H_2O$ – Dinâmica, 95%) (for obtain materials with $x = 0$) or calcium nitrate ($Ca(NO_3)_2.4H_2O$ – Synth, 99%) (for obtain materials with $x = 1.0$) was added to system and left stirring for another 5 min. To obtain materials with $x = 0.5$, the nitrates of lanthanum and calcium are added at same time. Soon after, the system temperature was raised to 70 °C to then slowly add the chelating agent collagen (Nutrigold do Brasil), the temperature required for better dissolution of this. This done, the system was kept under agitation for another 30 min. The obtained solution was then concentrated in an oven at 120 °C for 2 h and then pre-calcined in a muffle furnace, under following heating schedule: from 30 to 120 °C, remaining for 30 min; from 120 to 250 °C, remaining for 30 min; from 250 to 350 °C, remaining for 1 h. This procedure was done under a heating rate of 5 °C/min. A material with brittle consistency was obtained, which was broken and then calcined at 700 °C for 2 h, under 10 °C/min heating rate. Three dark powder solids were obtained: $CaMnO_3$ (CMO), $La_{0.5}Ca_{0.5}MnO_3$ (LCMO) and $LaMnO_3$ (LMO).

Characterization of $La_{1-x}Ca_xMnO_3$

X-ray analysis were recorded by PANAnalytical analyser with Empyrean CuLFF x-ray tube performed under radiation Cu-Kα ($\lambda = 0.15406$ nm), with scanning step of 0.026°, scanning range of 15°–60°, under tension of 40 Kv and current of 40 mA. The crystallite size was calculated using the Scherrer Equation applied in the structure main peak (Tavakkoli & Yazdanbakhsh 2013; Sanaeishoar *et al.* 2014; Tabari *et al.* 2017). The specific surface areas (S_{BET}) were determined by nitrogen adsorption–desorption using Brunauer–Emmett–Teller (BET) method. The total pore volumes and pore diameter were calculated in the desorption branch of isotherm, applying Barrett–Joyner–Halenda (BJH) method. The N_2 physisorption isotherms were built in MICROMERITICS equipment, ASAP model, at 77 K. FTIR analyses were recorded by SHIMADZU equipment, IR-PRESTIGE model, obtained on wavenumber range between 4,000 and 400 cm^{-1}, using the KBr pellet method. The materials surface texture was analyzed using HITACHI scanning electron microscopy, model TM 3,000, with magnification of 800x to LMO and LCMO and 500x to CMO. The PZC was done based by equilibrium method in a bath system, proposed by

Smiciklas *et al.* (2000), in the pH value on that difference between pH before and after the experiment is zero. Data linear regression provides the most appropriate value. All experiments were made at room temperature (23 °C).

Adsorption tests

Before adsorption tests, dye analytical curve was built and its photodegradation study was carried out. The analytical curve (Fig. S1) purpose is obtain the maximum absorbance of solution as a concentration function. The photodegradation study (Fig. S2) was done to assess whether dye solution is stable under adsorption tests experimental conditions (laboratory brightness, temperature, degree of agitation), but in the adsorbent absence. Both experiments are used to obtain the dye characteristic wavelength. For more details, see the Supplementary Material. The commercial dye studied, BB, was obtained from a local textile industry.

Then, the adsorption tests were carried out in batch mode, single stage, in which removal kinetics and adsorption equilibrium of dye solutions with 10, 30 and 50 ppm (mg/L) initial concentrations were evaluated. Before experiments, the adsorbents were dried in an oven at 80 °C for 30 min. In erlenmeyer flasks, 20 mg of adsorbent were contacted with 20 mL of dye solution, under stirring and at room temperature (23 °C). Dye removal was evaluated at following times: 10, 20, 30, 40, 50, 60, 70, 80 and 90 min. At the end of each time, the adsorbents loaded with dye were removed by filtration with qualitative paper-filter and centrifugation at 3,500 rpm for 5 min. The resultant solution absorbance was measured in the spectrophotometer at wavelength $\lambda = 601$ nm, referring to dye maximum absorbance (see Fig. S2). The adsorption experiments were carried out in triplicate with the solution at an initial pH adjusted to 3. This value was chosen because the PZC's results and preliminary tests carried out revealed that removal capacity increases with decreasing the solution pH. The solution concentration, adsorption capacity (or adsorbate concentration in the adsorbent) and removal efficiency were calculated using Equations (1)–(3), respectively. Figure 1 shows the methodology of adsorption tests and regeneration study.

$$C = C_0\left(\frac{A}{A_0}\right) \tag{1}$$

$$q = \frac{(C_0 - C)V}{m} \tag{2}$$

$$E(\%) = \left(\frac{C_0 - C}{C_0}\right) \times 100\% \tag{3}$$

where C represents the dye concentration in the solution (mg/L), A the absorbance, V the solution volume (L), m the adsorbent mass (g) and q the amount of dye adsorbed by the adsorbent (mg/g). The sub-index zero represents the values for initial time (zero), in the adsorbent absence. This experimental data was used in kinetic and equilibrium studies.

Regeneration and reuse study

The adsorbent loaded with dye, recuperated of adsorption tests, was dried in an oven at 80 °C to then be regenerated by heating to 700 °C, under the same calcination condition used in adsorbent synthesis, in order to decompose the adsorbed dye and recover the adsorbent. This temperature and methodology for the regeneration of the adsorbent was chosen based on previous studies (Santos *et al.* 2018; Ribeiro 2019; Souza 2019). Then, the regenerated adsorbent was reused five times, using consecutive masses of 100, 80, 60, 40 and 20 mg. The reuses were carried out under same conditions as adsorption tests, but only for the time of 90 min. The reuse study employed three concentrations (10, 30 and 50 ppm), but for the last two, only one reuse, with 20 mg, was done (Figure 1). The SHIMADZU UV-visible Spectrophotometer, UV-1,800 model, was used to obtain analytical curve and to do the photodegradation study and the adsorption and regeneration tests.

RESULTS AND DISCUSSION

Characterization of adsorbents

The LMO XRD pattern (Figure 2), available in Nascimento *et al.* (2020), confirmed the achievement of orthorhombic $LaMnO_3$ perovskite phase (ICSD n° 82,226; Chen *et al.* 2013; Sanaeishoar *et al.* 2014; Farhadi *et al.* 2017). A small relative amount of manganese oxide II (ICSD n° 643,195) was also observed as secondary phase. This oxide was probably generated by excess of manganese reagent which, at high calcination temperature and in contact with common atmosphere oxygen, was converted to manganese oxide II, maintaining oxidation state of its respective reagent. The LCMO XRD pattern (Figure 2) showed only orthorhombic $La_{0.5}Ca_{0.5}MnO_3$ perovskite phase (ICSD n° 155,406; González-Calbet *et al.* 1999; Walha *et al.* 2007; Mahata *et al.* 2017; Mo *et al.* 2018; Ben Moumen *et al.* 2019), confirming the mixed oxide obtaining. Both oxides obtained have nanometric crystallite size (Table 1).

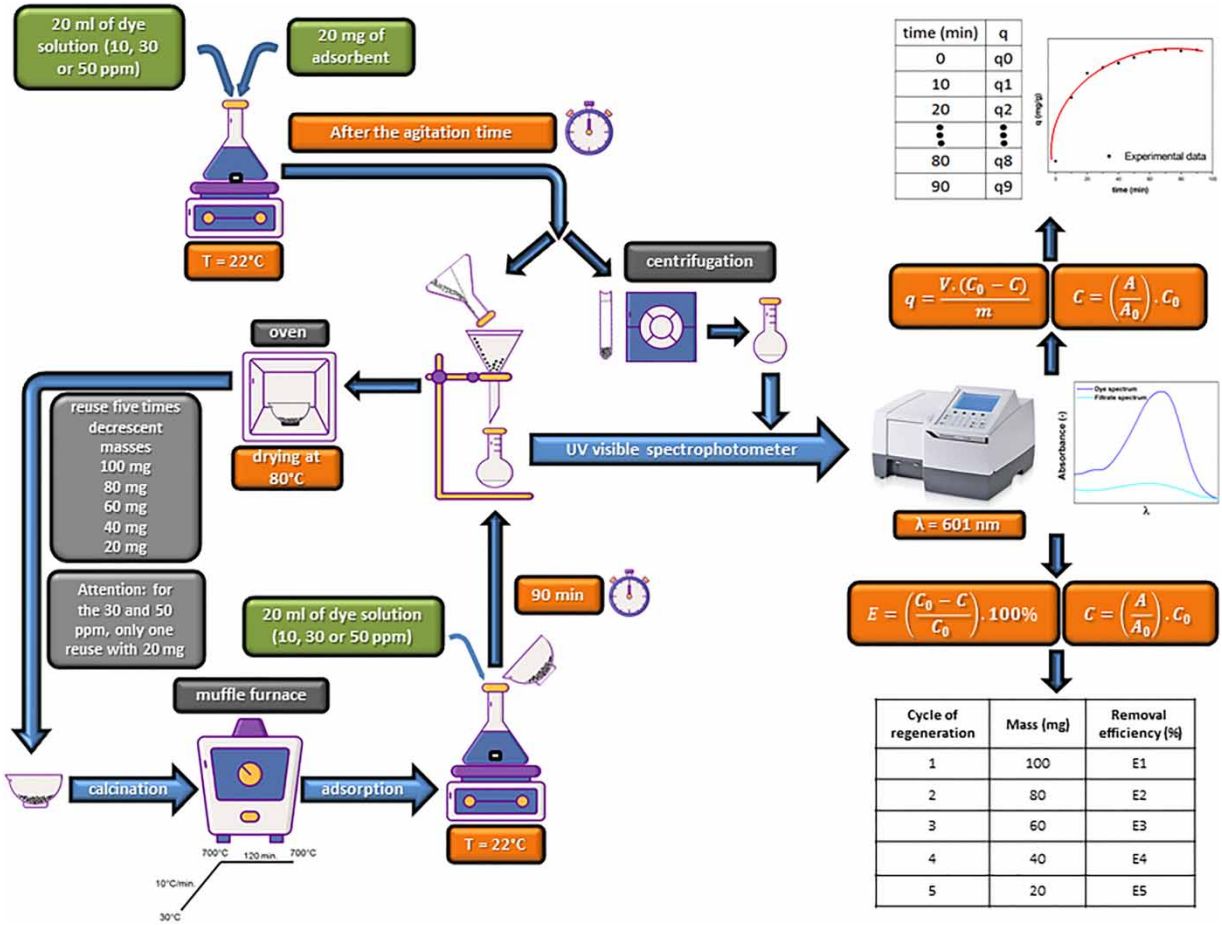

Cycle of regeneration	Mass (mg)	Removal efficiency (%)
1	100	E1
2	80	E2
3	60	E3
4	40	E4
5	20	E5

Figure 1 | Methodology of the adsorption tests and regeneration study.

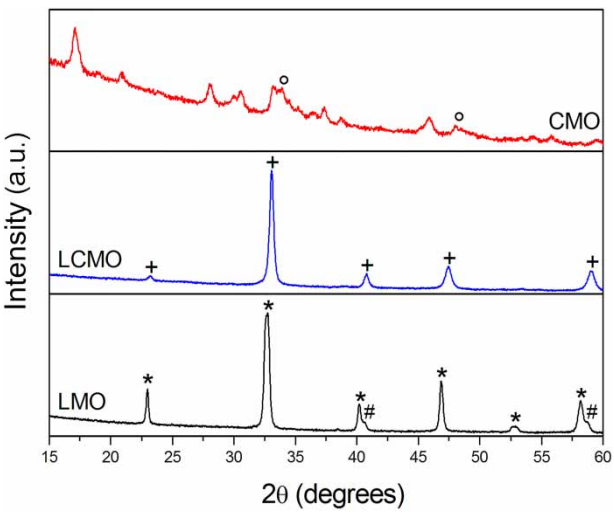

Figure 2 | XRD patterns for LMO (Nascimento *et al.* 2020), LCMO and CMO. $LaMnO_3$ (*), $La_{0.5}Ca_{0.5}MnO_3$ (+), $CaMnO_3$ (°), MnO (#).

Comparing LMO and LCMO diffractograms, it is noted that doping with calcium promoted a small displacement of peaks to greater angles and the disappearance of peak located at 53°. This variation is subtle because of Ca^{2+} (114 $\dot{A}$) and La^{3+} (117.2 $\dot{A}$) ions radii are similar. In addition, there was an increase in crystallite size, 18 to 23.7 nm (Table 1), caused by the emergence of oxygen vacancies, generated to compensate the structure loads,

Table 1 | Structural and textural properties of synthesized adsorbents

	LMO	LCMO	CMO
Crystal size (nm)	18.0	23.7	–
S_{BET} (m^2/g)	7	12	11
Total pore volume (cm^3/g)	0.0674	0.1165	0.0599
Pore diameter (nm)	38.2	41.5	29.0
PZC	7.5	7.7	9.0

unbalanced due to incorporation of a cation (Ca^{2+}) with a lower charge than pre-existing metal (La^{3+}) (Tavakkoli *et al.* 2014; Tabari *et al.* 2017). Compared to other works like of Tavakkoli *et al.* (2014) (750 °C/9 h), Mahata *et al.* (2017) (800 °C/12 h) and Ben Moumen *et al.* (2019) (850 °C/8 h), the synthesis method employed achieved synthesized crystalline and practically monophasical perovskites employing a low cost chelating agent and a relative softer calcination condition.

The CMO XRD pattern (Figure 2) presents several poorly defined peaks with low intensity, in addition to a lot of noise and an inclined baseline. This means that a cohesive and well-defined single-phase structure was not obtained, but an aggregate of compounds. In addition, it is possible that there are still products from synthesis precursors that are not desired phase. The comparison with ICSD n° 258,991 crystallographic chart indicates that peaks present at angular positions 34° and 48.8° refer to orthorhombic $CaMnO_3$. However, these are not the most intense of diffractogram, nor are they well defined. The most intense diffractogram peak, located around 17.4°, can be indexed to reagent $Ca(NO_3)_2.4H_2O$ (ICDD 156,304) and to compound $Ca(NO_2)_2.4H_2O$ (ICDD-PDF 00-038-0636). This indicates that part of reagents was not reacted during the synthesis, suggesting that perovskite phase formation has only just started. The other peaks present in the diffractogram refers to calcium and manganese II oxides, mostly the first. The most likely explanation is that the calcination condition employed (700 °C/2 h) was not sufficient to generate monophasic and crystalline $CaMnO_3$ perovskite. This explanation is supported by literature, as no study used a temperature less than 800 °C to obtain $CaMnO_3$ (Muro *et al.* 2005; Du *et al.* 2014; Han *et al.* 2014a, 2014b; Goian *et al.* 2015; Mo *et al.* 2018).

The BB XRD pattern (Fig. S3) shows a crystalline structure presence with several well-defined peaks that refer to sodium sulfate (ICDD 81,506) and sodium chloride (ICDD 169,462) presence. However, it is important to note that dyes are complex organic structures. Therefore, these two inorganic compounds are not only dye constituents, but they are the most crystallines. Another important point is that some compounds with sodium practically have peaks at angular positions 31.8° and 45.5°. Therefore, there is a possibility that sodium compound is not sodium chloride. The sulfate presence in considerable quantity indicates the dye is reactive. The XRD is quite similar to that obtained by Rodrigues (2016) for the same dye. There is little information available about this dye.

The dye FTIR spectrum (Figures 3–5) showed three characteristic bands: the first around 3,447 cm^{-1}, related to

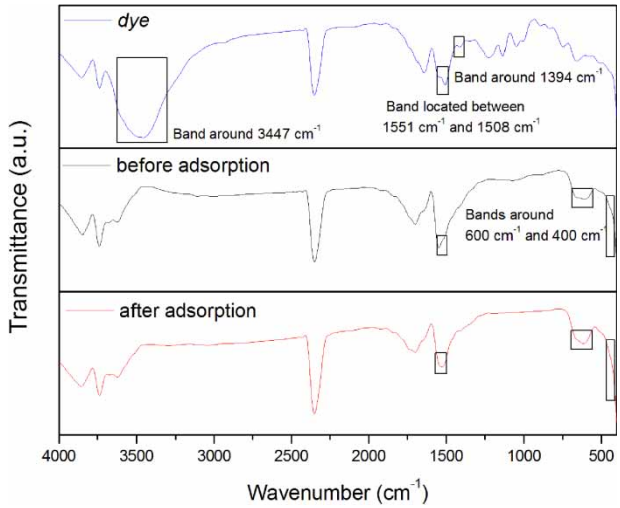

Figure 3 | FTIR spectra for BB (dye) and LMO before and after adsorption.

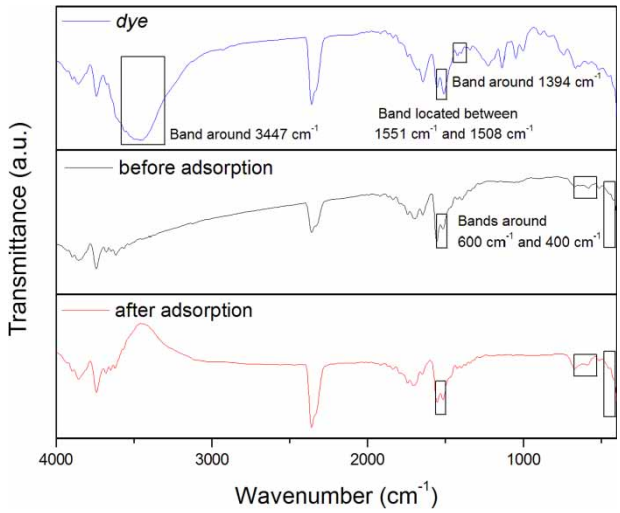

Figure 4 | FTIR spectra for BB (dye) and LCMO before and after adsorption.

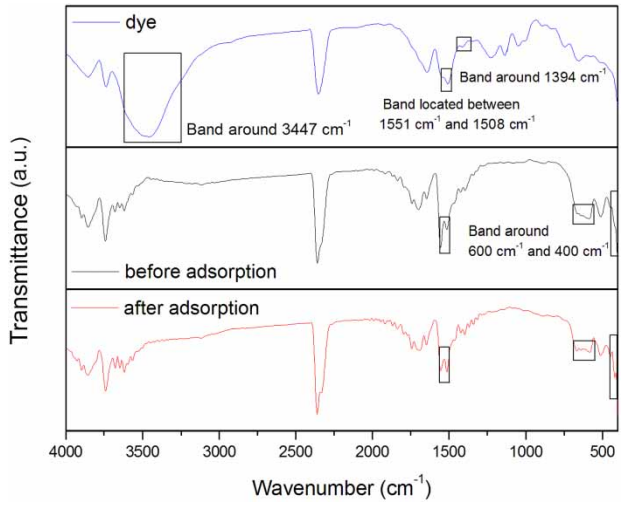

Figure 5 | FTIR spectra for BB (dye) and CMO before and after adsorption.

O-H bond stretching, probably present due to physically adsorbed water, the second between 1,551 and 1,508 cm^{-1}, referring to C = N bond symmetrical stretching, and the third around 1,394 cm^{-1}, referring to symmetrical stretching of C = N groups present in the aromatic ring (Rodrigues 2016). Figure 3 also is available in Nascimento *et al.* (2020).

The adsorbents spectra (Figures 3–5) show bands around 600 and 400 cm^{-1}, characteristics of metal-oxygen bonds. In the case of perovskite oxides well synthesized, LMO and LCMO, these bands are related to υ M-O bonds stretching and δ M-O-M bonds vibration modes, respectively (Hashemian & Foroghimoqhadam 2014; Tavakkoli & Moayedipour 2014; Tavakkoli *et al.* 2014; Farhadi *et al.* 2017). For CMO, these bands are related to metal-oxygen bonds of precursor oxides and also of perovskite phase.

The only evidence that adsorbent is loaded with dye is the slight elongation of band located between 1,551 and 1,508 cm^{-1}. The probable explanation for the dye characteristics bands absence in loaded adsorbent spectrum is due to the low concentration of dye solution employed, resulting in a small absolute amount of adsorbed dye. The characteristic bands maintained their position and intensity, indicating the oxides maintained its structure after adsorption process. This fact suggests the adsorption did not occur through strong interactions, implying a regeneration process that can remove/decompose adsorbate without destroying adsorbent structure will maintain the perovskite adsorptive capacity (Nascimento *et al.* 2020).

The synthesized materials shown low specific area (Table 1), something already indicated by literature (Zhu *et al.* 2014; Tabari *et al.* 2017; Mo *et al.* 2018; Santos *et al.* 2018; Fernandes *et al.* 2020). In addition, the pore diameter classifies them as mesoporous, which must be linked to agglomerated nanoparticles formation (Mo *et al.* 2018). The doped oxide showed higher specific superficial area (S_{BET}), total pore volume and pore diameter, which may be due to pores formation in stacked crystal particles (Mo *et al.* 2018).

The three N_2 physisorption isotherms (Figures 6–8) are characteristic of macroporous or nonporous materials, and have a hysteresis loop, typical of systems composed by particles aggregates in plate or lamella forms, generating pores with a slit or cavity shape (Thommes *et al.* 2015), in agreement with stated by Mo *et al.* (2018). This same profile (similar isotherms and hysteresis) has been presented by other studies with perovskite oxides (Du *et al.* 2014; Han *et al.* 2014b; Sanaeishoar *et al.* 2014; Ding *et al.* 2017; Tabari *et al.* 2017; Mo *et al.* 2018). The pore diameter distribution curves for LMO and LCMO (inset of Figures 6 and 7) confirm the meso and macropores presence, mostly mesopores. The fact these curves are continuous and have only a maximum region indicates the materials structure is organized, with pores diameter in a narrow values range. The same is not shown by pore diameter distribution curves for CMO (inset of Figure 8), confirming that the structure obtained is not organized and has pores/cracks with varying diameters, something already indicated by XRD (Figure 2).

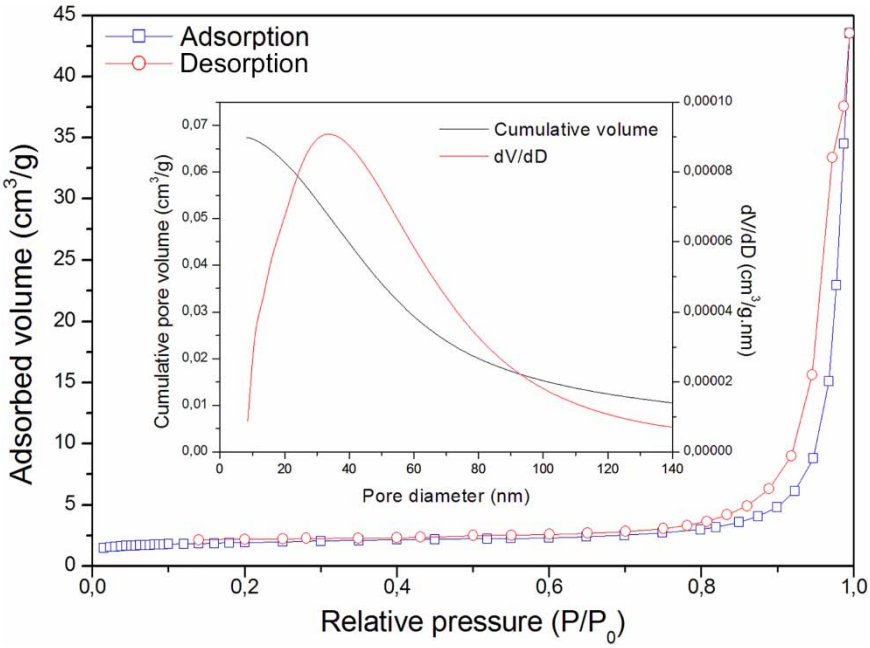

Figure 6 | Nitrogen adsorption isotherm and corresponding pore diameter distribution curves (inset) of LMO.

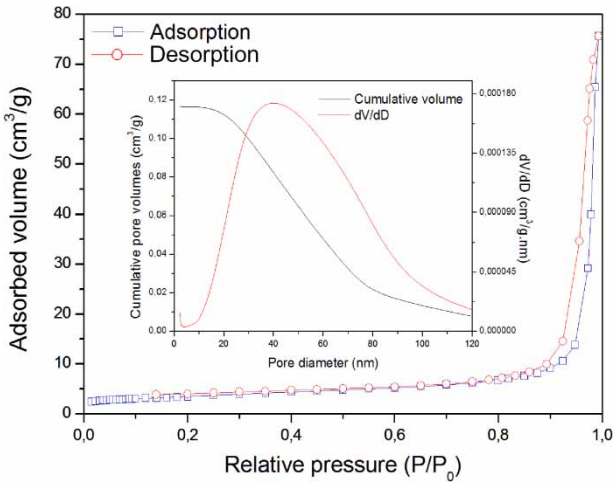

Figure 7 | Nitrogen adsorption isotherm and corresponding pore diameter distribution curves (inset) of LCMO.

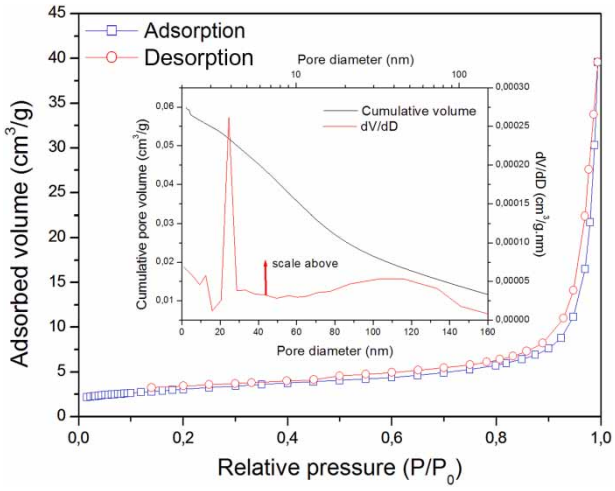

Figure 8 | Nitrogen adsorption isotherm and corresponding pore diameter distribution curves (inset) of CMO.

The LMO and LCMO PZCs are around neutrality (Table 1), similar to other literature works that have studied homologous materials (Couto *et al.* 2020; Fernandes *et al.* 2020; Ribeiro *et al.* 2020). Thus, contact with acidic solutions leaves the net surface charge of adsorbent positive while contact with basic solutions leaving the adsorbent surface with negative net charge. Preliminary tests carried out revealed that removal capacity increases with decreasing the solution pH. That is, the more positive the adsorbent surface is, greater the dye removal. This is a strong indication that dye is anionic when in aqueous solution. The CMO PZC is equal to 9.0 (Table 1). This difference in relation to other adsorbents is probably due to CMO was not constituted predominantly by $CaMnO_3$ oxide, but by a mixture of oxides with low crystallinity, as seen in XRD (Figure 2). The PCZ increase with calcium entry into structure may be related to the fact that doping promotes partial replacement of La^{3+} cation by Ca^{2+}, generating anionic vacancies in structure.

The SEM images (Figure 9) show that synthesized adsorbents have an irregular, spongy and rough surface, with many cavities and little agglomeration, mainly of small particles, which must have grown on larger ones. In addition, the particles have varying sizes and shapes. This helps to explain the good adsorptive behavior. The same was seen in some works in literature (Oliveira *et al.* 2010; Tavakkoli & Yazdanbakhsh 2013; Han *et al.* 2014b; Mo *et al.* 2018; Rakass *et al.* 2018; Farhadi & Mahmoudi 2019; Lemos *et al.* 2020; Ribeiro *et al.* 2020). The porous structure was probably favored during synthesis, in the gases released from chelating agent decomposition (Oliveira *et al.* 2010).

Adsorption tests

The dye analytical curve (Fig. S1) shows that it complies with Beer's Law, with mass absorptivity equal to 24.9 $L{\cdot}cm^{-1}{\cdot}g^{-1}$, and has a characteristic wavelength equal to 601 nm. The photodegradation study (Fig. S2) reveals that dye solution is stable under experimental conditions.

In general, perovskite type oxides have low specific areas, with better results in processes involving surface interactions and/or electron transfer (Zhu *et al.* 2014). Therefore, there was not evaluated kinetic models that consider internal diffusion stage in adsorbent. Then, only pseudo-first- (PFO) and pseudo-second- (PSO) order models, both formulated considering adsorptions stage on sites as slowest in the process (Ho & McKay 1999; Febrianto *et al.* 2009; Largitte & Pasquier 2016), were evaluated. In addition, these two models (Equations (4) and (5), respectively) are the most applied to study dyes adsorption on perovskite oxides to date (Yazdanbakhsh *et al.* 2011; Farhadi *et al.* 2017; Santos *et al.* 2018; Farhadi & Mahmoudi 2019; Couto *et al.* 2020; Fernandes *et al.* 2020; Lemos *et al.* 2020; Nascimento *et al.* 2020).

$$q = q_e(1 - e^{-k_1 t}) \tag{4}$$

$$q = \frac{k_2 q_e t}{1 + k_2 q_e t} \tag{5}$$

where q and q_e are the adsorption capacities (or concentration in the adsorbent) at a time t and in equilibrium,

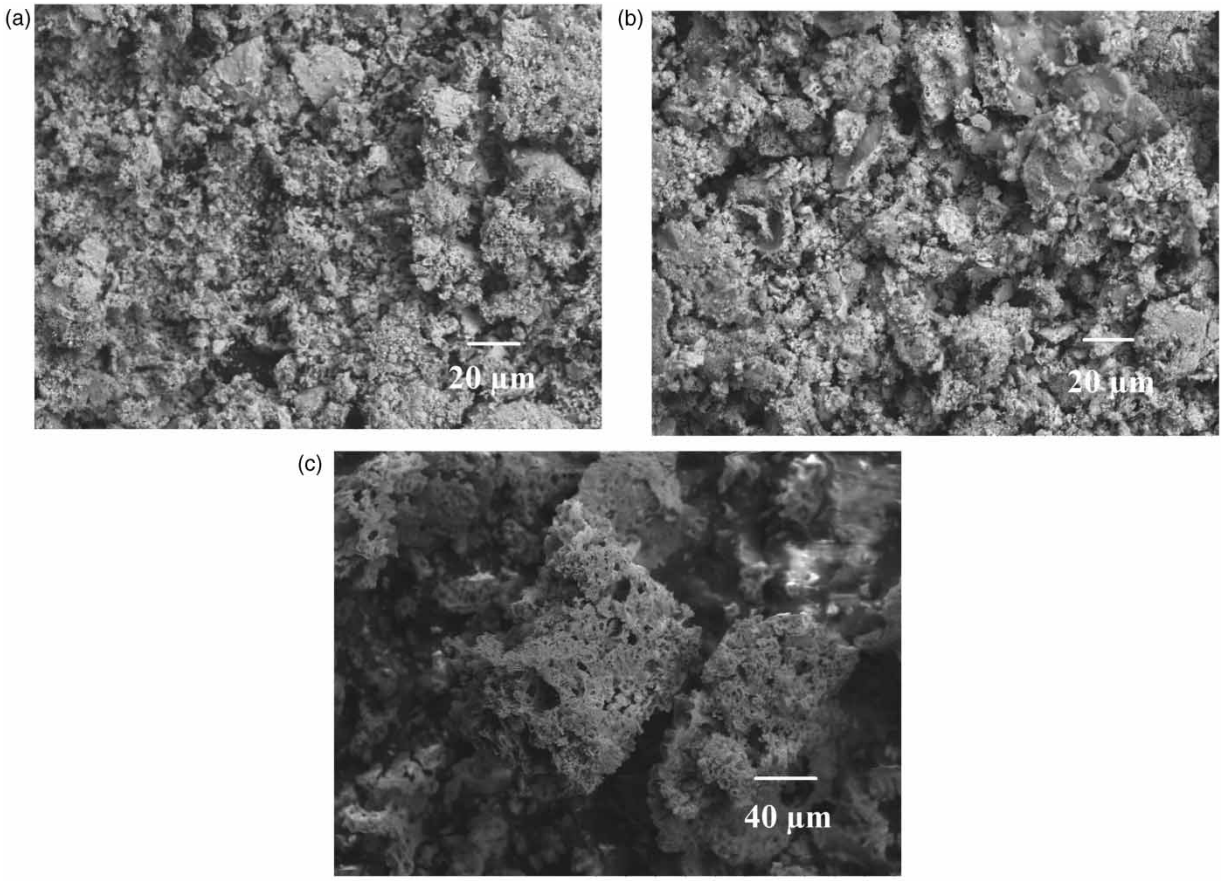

Figure 9 | SEM images for LMO (a), LCMO (b) and CMO (c).

respectively, and k_1 and k_2 are the adsorption rate constants of pseudo-first- and pseudo-second-orders, respectively. These parameters were calculated by non-linear regression of experimental data to Equations (4) and (5).

The graphs (Figures 10–12) and Table 2 analysis shows that LMO and LCMO performed well, especially for 10 and 30 ppm initial concentrations. For CMO, a less effective behavior occurred, probably due to not being made up of perovskite monophase. In addition, it can be said that doping with calcium makes adsorbents less effective and slower (less kinetic constant). The PSO model is one that best describes the process kinetic behavior in all cases, although PFO model also provides reliable results. This evaluation was made based on R^2 (linear correlation coefficient) and χ^2 (Pearson correlation coefficient) fitting parameters and comparing experimental and estimated q_e.

The PSO model was formulated considering that process limiting step is an adsorption mechanism (Aksu & Tezer 2000), which can be a chemisorption, where an electrons exchange or sharing occurs between adsorbent and adsorbate

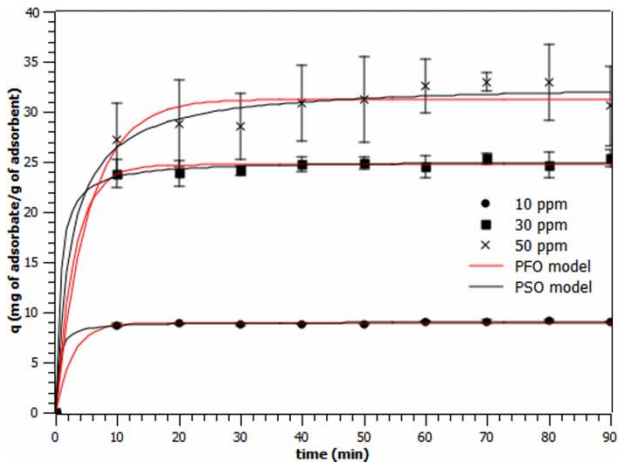

Figure 10 | Non-linear regression curves of LMO adsorbent to PFO and PSO models.

(Ho & McKay 1999). Therefore, the results are physically based, after all, as previously mentioned, the processes involving perovskite oxides occur mainly through electron transfer and/or surface interactions, after all, they are little porous

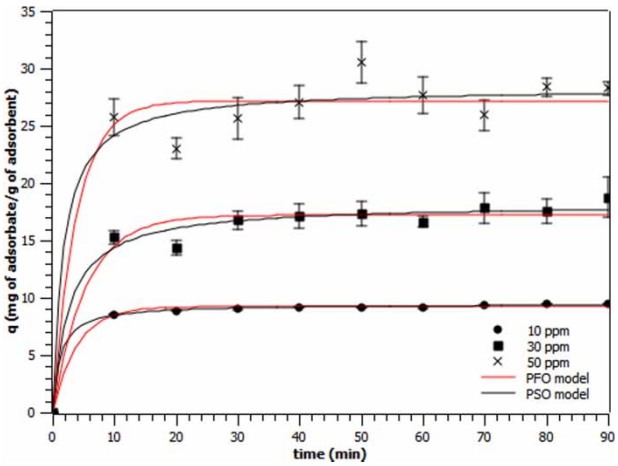

Figure 11 | Non-linear regression curves of LCMO adsorbent to PFO and PSO models.

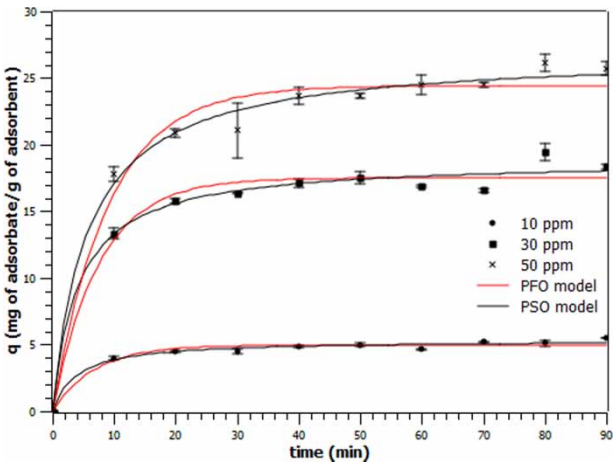

Figure 12 | Non-linear regression curves of CMO adsorbent to PFO and PSO models.

structures (Zhu *et al.* 2014), with electrostatic attraction between dye molecules and adsorbent surface being the predominant mechanism (Al-Degs *et al.* 2008; Yazdanbakhsh *et al.* 2011; Tavakkoli & Moayedipour 2014; Tavakkoli *et al.* 2014; Farhadi & Mahmoudi 2019).

The results also show that initial concentration increases promote an adsorption capacity (q_e) increase and a decrease in removal efficiency and adsorption rate kinetic constant. These same conclusions were obtained by other literature works (Yazdanbakhsh *et al.* 2011; Farhadi *et al.* 2017; Farhadi & Mahmoudi 2019). The removal percentage decrease occurs due to adsorption sites saturation. As for kinetic constant, although mass gradient between phases (that is, the difference between adsorbent concentration at equilibrium and a time t $(q - q_e)$), and the removal rates are higher at higher initial concentrations, it should be kept in mind that a higher initial concentration will promote dye molecules competition for adsorption sites, slowing down the process. In addition, these molecules' length and volume can be large enough to promote stereochemical impediment when linked to adsorptive sites, making it difficult to adsorb other molecules to neighboring sites and thus slowing down the process. Another explanation, given by Hashemian & Foroghimoqhadam (2014), states this phenomenon probably occurs due to electrostatic repulsion between adsorbed anionic dye molecules and those present in solution. All this analysis is valid for LMO and LCMO. For CMO, although initial concentration increase has decreased adsorption kinetic constants values, the removal percentage showed an unusual behavior, probably due to adsorbent being composed by a cluster of different oxides.

The adsorption kinetic constant is a parameter that depends not only the initial concentration, but also on other experimental conditions, such as agitation degree and system temperature. In addition, it is also a function of adsorbent–adsorbate interaction and adsorbents properties, such as porosity and surface morphology. As an example of this last factor, Fernandes *et al.* (2020) synthesized $LaNiO_3$ using three different methodologies and used it to remove Congo Red. The results showed that presented kinetic constant was different, although materials obtained were the same, but obtained by different methods and, therefore, presented textural properties that were also different. In addition, it was noted that initial concentration increase promoted higher error bars. The probable explanation must be the same as kinetic constant behavior. Another explanation is that adsorbent surface coverage is heterogeneous, which can facilitate/hinder adsorption of new molecules, generating more random results that were evident in higher initial concentrations.

Compared to other studies that used $LaMnO_3$ as a dye adsorbent, the LMO performed better (Table 3), removing a higher percentage in shorter contact time. The adsorbent-adsorbate interactions must be favorable to BB dye. These results also show that synthesis method chosen is effective, as it produced a material with greater adsorptive capacity under milder synthesis conditions and employing a cheaper complexing agent (collagen).

The adsorption equilibrium was evaluated using Langmuir and Freundlich models in their linear forms (Equations (6) and (7)), where q_{max} is the adsorption capacity (or adsorbent concentration) of saturated monolayer, C_e is the equilibrium adsorbate concentration in the liquid phase, K_L is the adsorption equilibrium constant, also known as the Langmuir constant, K_F is the

Table 2 | Kinetic parameters estimated in data nonlinear regression and removal efficiency values

Adsorbent	Initial conc. (ppm)	PFO	PSO	Removal efficiency (%)
LMO	10	$q_e = 8.953 \pm 0.042$ mg/g $k_1 = 0.362 \pm 0.052$ min^{-1} $R^2 = 0.998$ $\chi^2 = 0.0136$	$q_e = 9.046 \pm 0.049$ mg/g $k_2 = 0.255 \pm 0.082$ g·mg^{-1}·min^{-1} $R^2 = 0.999$ $\chi^2 = 0.0085$	92
	30	$q_e = 24.711 \pm 0.172$ mg/g $k_1 = 0.323 \pm 0.052$ min^{-1} $R^2 = 0.997$ $\chi^2 = 0.2323$	$q_e = 25.118 \pm 0.189$ mg/g $k_2 = 0.058 \pm 0.017$ g·mg^{-1}·min^{-1} $R^2 = 0.998$ $\chi^2 = 0.1254$	85
	50	$q_e = 31.229 \pm 0.558$ mg/g $k_1 = 0.188 \pm 0.033$ min^{-1} $R^2 = 0.979$ $\chi^2 = 2.2654$	$q_e = 32.831 \pm 0.657$ mg/g $k_2 = 0.013 \pm 0.003$ g·mg^{-1}·min^{-1} $R^2 = 0.989$ $\chi^2 = 1.2152$	63
LCMO	10	$q_e = 9.226 \pm 0.066$ mg/g $k_1 = 0.252 \pm 0.026$ min^{-1} $R^2 = 0.996$ $\chi^2 = 0.0334$	$q_e = 9.470 \pm 0.052$ mg/g $k_2 = 0.089 \pm 0.012$ g·mg^{-1}·min^{-1} $R^2 = 0.999$ $\chi^2 = 0.0089$	95
	30	$q_e = 17.201 \pm 0.408$ mg/g $k_1 = 0.185 \pm 0.042$ min^{-1} $R^2 = 0.964$ $\chi^2 = 1.2090$	$q_e = 18.191 \pm 0.500$ mg/g $k_2 = 0.021 \pm 0.007$ g·mg^{-1}·min^{-1} $R^2 = 0.979$ $\chi^2 = 0.6844$	63
	50	$q_e = 27.162 \pm 0.750$ mg/g $k_1 = 0.257 \pm 0.106$ min^{-1} $R^2 = 0.949$ $\chi^2 = 4.3161$	$q_e = 28.323 \pm 1.046$ mg/g $k_2 = 0.020 \pm 0.013$ g·mg^{-1}·min^{-1} $R^2 = 0.961$ $\chi^2 = 3.3496$	56
CMO	10	$q_e = 4.971 \pm 0.112$ mg/g $k_1 = 0.145 \pm 0.025$ min^{-1} $R^2 = 0.969$ $\chi^2 = 0.0848$	$q_e = 5.346 \pm 0.136$ mg/g $k_2 = 0.048 \pm 0.012$ g·mg^{-1}·min^{-1} $R^2 = 0.984$ $\chi^2 = 0.0442$	55
	30	$q_e = 17.487 \pm 0.371$ mg/g $k_1 = 0.133 \pm 0.020$ min^{-1} $R^2 = 0.974$ $\chi^2 = 0.9031$	$q_e = 18.865 \pm 0.505$ mg/g $k_2 = 0.012 \pm 0.003$ g·mg^{-1}·min^{-1} $R^2 = 0.983$ $\chi^2 = 0.5800$	63
	50	$q_e = 24.426 \pm 0.546$ mg/g $k_1 = 0.110 \pm 0.015$ min^{-1} $R^2 = 0.973$ $\chi^2 = 1.819$	$q_e = 26.876 \pm 0.543$ mg/g $k_2 = 0.006 \pm 0.001$ g·mg^{-1}·min^{-1} $R^2 = 0.991$ $\chi^2 = 0.5662$	53

characteristic constant related to the adsorption capacity, also known as the Freundlich constant, n is the characteristic constant related to adsorption intensity, or favorability degree of adsorption (Vijayaraghavan *et al.* 2006; Chatterjee *et al.* 2007; Febrianto *et al.* 2009; Hashemian & Foroghimoqhadam 2014; Aljeboree *et al.* 2017). These parameters were determined by plotting the curve C_e/q_e vs C_e in Equation (6) and $ln\ q_e$ vs $ln\ C_e$ in Equation (7).

$$\frac{C_e}{q_e} = \frac{1}{K_L q_{\max}} + \left(\frac{1}{q_{\max}}\right) C_e \tag{6}$$

$$\ln q_e = \ln K_F + \left(\frac{1}{n}\right) \ln C_e \tag{7}$$

The Langmuir model is the one that best represents adsorption equilibrium when used the LMO adsorbent while Freundlich model is most suitable for LCMO and CMO (Table 4). The Freundlich isotherm is applicable to almost all experimental adsorption–desorption systems, especially for those highly heterogeneous, or that have varying affinity (Vijayaraghavan *et al.* 2006; Febrianto *et al.* 2009), this being the probable explanations for its adjustment to CMO, a material composed by an agglomerate of oxide phases. The monolayer adsorption capacity values (q_{max}) (Table 4) presented are in accordance with this new adsorbents class (Yazdanbakhsh *et al.* 2011; Tavakkoli & Moayedipour 2014; Farhadi & Mahmoudi 2019). Doping with calcium reduced this parameter, making

Table 3 | Comparative use of $LaMnO_3$ as adsorbent

Synthesis method	Dye	Initial conc.	Equilibrium time	Removal efficiency	Reference
MP	BB	10 ppm	90 min	92%	This work and Nascimento *et al.* (2020)
MP	BB	30 ppm	90 min	85%	This work
MP	BB	50 ppm	90 min	63%	This work
AC	MB	25 ppm	240 min	43%	Farhadi *et al.* (2017)
AC	MO	25 ppm	240 min	9%	Farhadi *et al.* (2017)
MP	CR	50 ppm	120 min	63%	Santos *et al.* (2018)

Note: MP, Modified proteic; AC, Auto combustion; MB, Methylene Blue; MO, Methyl Orange; CR, Congo Red.

Table 4 | Estimated parameters in linear regressions for equilibrium study

Langmuir

Adsorbent	q_{max} (mg/g)	K_L (L/mg)	R^2
LMO	33.75	0.54	0.999
LCMO	29.77	0.34	0.922
CMO	–	–	0.184

Freundlich

Adsorbent	n	K_F ($mg^{1-1/n} \cdot L^{1/n} \cdot g^{-1}$)	R^2
LMO	2.55	11.06	0.905
LCMO	3.64	10.97	0.958
CMO	1.05	1.45	0.933

adsorbent less effective, something already proven in kinetic studies.

The constant *n* (Table 4) indicates that the process is favorable to LCMO and has a linear behavior for CMO (Febrianto *et al.* 2009). Although they also indicate that process is physical (Febrianto *et al.* 2009; Aljeboree *et al.* 2017), it should be kept in mind that adsorption process on perovskite oxides very likely is chemical. Although they are materials with a low total area, the crystals' small size (Table 1) may have contributed to obtain meso and macropores in cracks and cavities shape. In addition, the relatively high pore diameters and volumes (Table 1) help explain the perovskites good performance as dye adsorbents, after all, they are bulky molecules. Therefore, in dye adsorption case, the three textural parameters, specific surface area, pore diameter and pore volume, must be taken into account instead of just a specific area. In addition, it should be kept in mind this materials class performance is a function of electronic exchanges and/or surface interactions (Zhu *et al.* 2014).

Regeneration and reuse tests

Figure 13 shows BB dye removal efficiencies for the LMO regeneration cycles. For the reuse of LMO adsorbent at 10 ppm dye initial concentration solution (Figure 13), the increase in removal percentages throughout reuses is due to the presence of more adsorptive sites in contact with dye (greater mass of adsorbent). However, comparing virgin adsorbent and last reuse, both with the same mass, it was found that adsorption capacity was maintained. When using the dye solution at 30 ppm and LMO material (Table 5), same affirmation can be done, but only in one cycle. However, for dye solution at 50 ppm, a considerable increase in removal percentage is observed (Table 5). The reason is that regeneration could have promoted structure recrystallization, after all, it is performed at the same calcination condition. So, more adsorptive sites may have appeared.

For LCMO material at 10 ppm dye initial concentration, adsorption occurred only for first reuse. Thereafter, the solution after process changed color from blue to purple, which

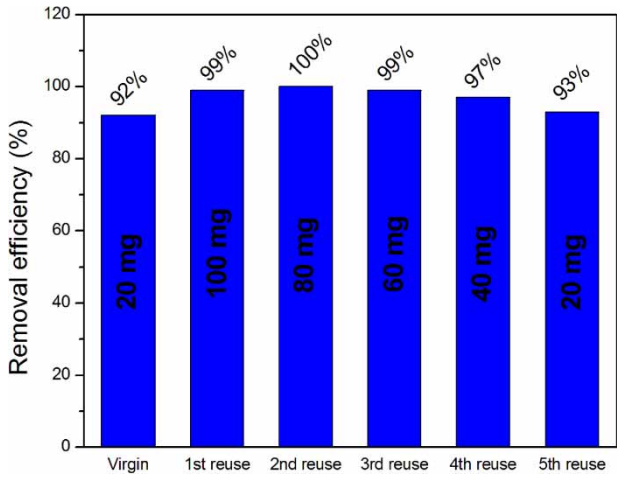

Figure 13 | Removal efficiency for LMO regeneration cycles.

Table 5 | Removal efficiency obtained in adsorbents reuse at 30 and 50 ppm

Adsorbent	Initial conc.	Virgin	1st reuse
LMO	30 ppm	85%	79%
	50 ppm	63%	80%
LCMO	30 ppm	63%	80%
	50 ppm	56%	80%
CMO	30 ppm	63%	77%
	50 ppm	53%	72%

weakened as the process progressed. In addition, the absorbance peak was dislocated for lowers wavelengths values (Figure 14). The conclusion is that after the regeneration process, adsorbent starts to act as a catalyst that increased its catalyst activity throughout regeneration cycles, because the absorbance curve intensity decreased. For 30 and 50 ppm initial concentrations, only adsorption occurs and both presented a higher removal than obtained value to the virgin adsorbent (Table 5). This increase can be also attributed to structure recrystallization that occurred in regeneration process.

For CMO, the results show that removal percentage increase throughout regeneration cycles and stabilized from third reuse onwards (Figure 15), probably due to $CaMnO_3$ phase consolidation. The comparison between virgin and fifth reuse show that percentages' increase did not occur because greater mass of adsorbent. At 30 and 50 ppm initial concentrations, removal percentages increased because same reason (Table 5). The results suggest that a phase with sites more active became more dominant in the material.

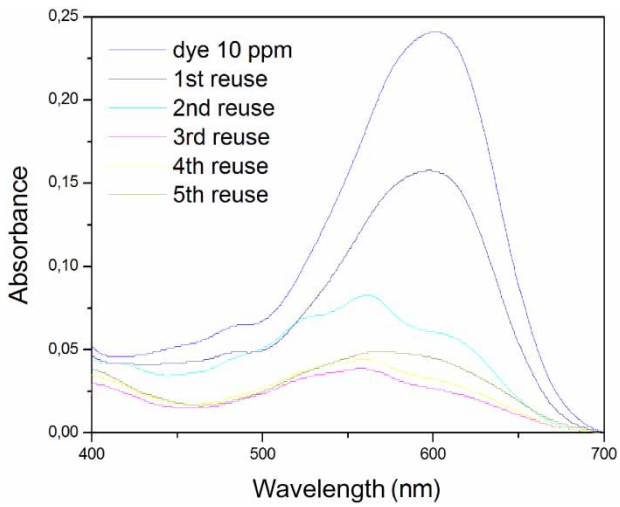

Figure 14 | Absorbance curves for dye 10 ppm solutions adsorbed by regenerated LCMO.

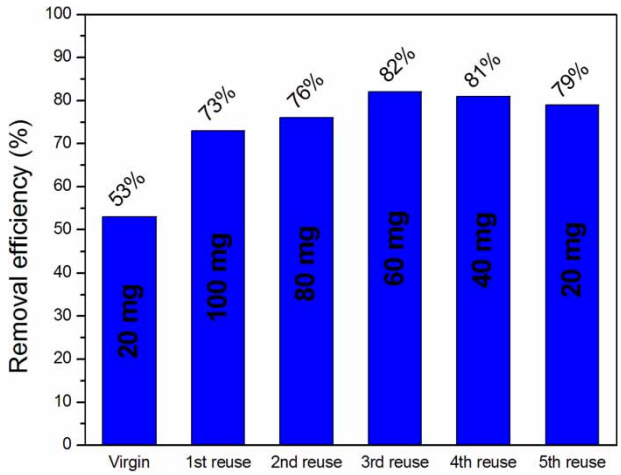

Figure 15 | Removal efficiency for CMO regeneration cycles.

The study of regeneration and reuse of adsorbent suggest that the adsorbent structure is free of the dye after the regeneration step, it is possible that this is an indication that the pores/cavities of material have a slit shape, as this format facilitates for the adsorbed molecules to leave.

Previous studies on the maintenance of the perovskite structure after dye adsorption tests, and calcination at temperatures above 700 °C, for material regeneration and reuse have indicated that this structure is stable and maintained after these conditions (Santos *et al.* 2018; Ribeiro 2019; Souza 2019). In addition, the efficiency of the adsorbent for new dye adsorption (reuse) tests has been reported to be increased in some cases.

CONCLUSIONS

The LMO and LCMO syntheses were successful, generating respective perovskite nanomaterials with orthorhombic structure. Compared to other works, the synthesis method employed achieved synthesized crystalline and practically monophasical perovskites employing a low cost chelating agent and a relatively softer calcination condition. The CMO synthesis did not generate a perovskite monophase due to low temperature and calcination time employed. FTIR spectra showed adsorption process does not damage adsorbent structure. All adsorbents synthesized have meso and macropores with slit or cavity shape. The adsorbents' surface is rough and have particles with different sizes and shapes. The LMO and LCMO PCZ is around neutrality and removal efficiency is better at acidic pHs, indicating the dye is anionic. The kinetic studies shows that PSO model is the one that best represents

the process. For equilibrium, Langmuir model best represent the process to LMO while Freundlich model was most adequate to other adsorbents. The regeneration process maintained LMO adsorptive capacity over five cycles.

Although they are materials with low specific surface area, the pore size is relatively large and the irregular and texturally rough surface explains the good adsorptive behavior. In addition, a complex electronic structure of perovskite type oxides must have attracted complex dye molecules. Even doped oxide has a good cost–benefit ratio, since calcium reagent is much cheaper than others, which has the best overall performance is LMO, as it presented a considerable adsorptive capacity and remained stable during all adsorption–regeneration cycles.

ACKNOWLEDGEMENTS

The authors are grateful at Conselho Nacional de Desenvolvimento Científico e Tecnológico (CNPq). This study was financed in part by the Coordenação de Aperfeiçoamento de Pessoal de Nível Superior – Brasil (CAPES) – Finance Code 001. In addition, the authors are grateful too at 'Flat Icons' for icons in some images.

DATA AVAILABILITY STATEMENT

All relevant data are included in the paper or its Supplementary Information.

REFERENCES

Aksu, Z. & Tezer, S. 2000 Equilibrium and kinetic modeling of biosorption of Remazol Black B by *Rhizopusarrhizus* in a batch system: effect of temperature. *Process Biochem.* **36**, 431–439.

Al-Degs, Y. S., El-Barghouthi, M. I., El-Sheikh, A. H. & Walker, G. M. 2008 Effect of solution pH, ionic strength, and temperature on adsorption behavior of reactive dyes on activated carbon. *Dyes Pigment.* **77**, 16–23. https://doi.org/10.1016/j.dyepig.2007.03.001.

Aljeboree, A. M., Alshirifi, A. N. & Alkaim, A. F. 2017 Kinetics and equilibrium study for the adsorption of textile dyes on coconut shell activated carbon. *Arab. J. Chem.* **10**, S3381–S3393. http://dx.doi.org/10.1016/j.arabjc.2014.01.020.

Attfield, J. P., Lightfoot, P. & Morris, R. E. 2015 Perovskites. *Dalton Trans.* **44**, 10541–10542. https://doi.org/10.1039/C5DT90083B.

Ben Moumen, S., Gagou, Y., Chettab, M., Mezzane, D., Amjoud, M., Fourcade, S., Hajji, L., Kutnjak, Z., El Marssi, M., El-Amraoui, Y., Kopelevich, Y. & Luk'yanchuk, I. A. 2019 Synthesis of $La_{0,5}Ca_{0,5-x}{}_xMnO_3$ nanocrystalline manganites by sucrose assited auto combustion route and study of their structural, magnetic and magnetocaloric properties. *J. Mat. Sci. Mat. Eletronics.* **30**, 20459–20470. https://doi.org/10.1007/s10854-019-02392-9.

Bestchem 2020 Available from: https://bestchem.hu/bestchem/en/surplus/product/22579 (accessed 1 February 2020).

Chatterjee, S., Chatterjee, S., Chatterjee, B. P. & Guha, A. K. 2007 Adsorptive removal of congo red, a carcinogenic textile dye by chitosan hydrobeads: binding mechanism, equilibrium and kinetics. *Coll. Surf. A-Physic. Eng. Asp.* **299** (1), 146–152. https://doi.org/10.1016/j.colsurfa.2006.11.036.

Chen, Y. H. 2011 Synthesis, characterization and dye adsorption of ilmenite nanoparticles. *J. Non-Cryst. Sol.* **357** (1), 136–139. https://doi.org/10.1016/j.jnoncrysol.2010.09.070.

Chen, J., Shen, M., Wang, X., Qi, G., Wang, J. & Li, W. 2013 The influence of nonstoichiometry on $lamno_3$ perovskite for catalytic NO oxidation. *Appl. Catal. B-Environ.* **134–135**, 251–257. http://dx.doi.org/10.1016/j.apcatb.2013.01.027.

Couto, J. E. N., Ribeiro, I. A., Garrido Pedrosa, A. M. & Souza, M. J. B. 2020 Synthesis of $LaFeO_3$ material for application in Congo Red dye removal by adsorption. In *13 Brazilian Meeting on Adsorption*, online, 30 November–3 December.

Ding, Y., Wang, S., Zhang, L., Chen, Z., Wang, M. & Wang, S. 2017 A facile method to promote $lamno_3$ perovskite catalyst for combustion of methane. *Catal. Commun.* **97**, 578–586. http://dx.doi.org/10.1016/j.catcom.2017.04.022.

Du, J., Zhang, T., Cheng, F., Chu, W., Wu, Z. & Chen, J. 2014 Nonstoichiometric perovskite $camno_{3-\delta}$ for oxygen electrocatalysis eith high activity. *Inorg. Chem.* **53**, 9106–9114. https://doi.org/10.1021/ic501631 h.

Farhadi, S. & Mahmoudi, F. 2019 Improving the adsorption ability of perovskite-type $lanio_3$ nanomaterial towards organic dyes by hybridizing with phosphotungstic acid. *Polyedron.* **169**, 39–50. https://doi.org/10.1016/j.poly.2019.05.008.

Farhadi, S., Mahmoudi, F., Amini, M. M., Dusek, M. & Jarosova, M. 2017 Synthesis and characterization of a series of novel perovskite-type $lamno_3$/Keggin-type polyoxometalate hybrid nanomaterials for fast and selective removal of cationic dyes from aqueous solutions. *Dalton Trans.* **46** (10), 3252–3264. https://doi.org/10.1039/C6DT04866H.

Febrianto, J., Kosasih, A. N., Sunarso, J., Ju, Y., Indraswati, N. & Ismadji, S. 2009 Equilibrium and kinetic studies in adsorption of heavy metals using biosorbent: a summary of recent studies. *J. Hazard. Mater.* **162**, 616–645. https://doi.org/10.1016/j.jhazmat.2008.06.042.

Fernandes, J. B. R., Souza, A. A., Ribeiro, I. A., Souza, M. J. B. & Garrido Pedrosa, A. M. 2020 Evaluation of LaNiO3 type materials prepared by different routes as adsorbent for dyes removal. In: *13 Brazilian Meeting on Adsorption*, online, 30 November–3 December.

Goian, V., Kamba, S., Borodavka, F., Nuzhnyy, D., Savinov, M. & Belik, A. A. 2015 The manifestation of spin-phonon coupling in $camno_3$. *J. Appl. Sci.* **117**, 164103-164103-6. https://doi.org/10.1063/1.4918659.

González-Calbet, J. M., Herrero, E., Rangavittal, N., Alonso, J. M., Martínez, J. L. & Vallet-Regi, M. 1999 Ordering of oxygen vacancies and magnetic properties in $La_{0,5}Ca_{0,5}MnO_{3-\delta}$ $(0 \leq \delta \leq 0.5)$. *J. Sol. S. C.* **148**, 158–168.

Han, X., Cheng, F., Zhang, T., Yang, J., Hu, Y. & Chen, J. 2014a Hydrogenated uniform Pt clusters supported on porous $CaMnO_3$ as a bifunctional electrocatalyst for enhanced oxygen reduction and evolution. *Adv. Mater.* **26**, 2047–2051. https://doi.org/10.1002/adma.201304867.

Han, X., Hu, Y., Yang, J., Cheng, F. & Chen, J. 2014b Porous perovskite $camno_3$ as an electrocatalyst for rechargeable Li-O_2 batteries. *Chem. Comm.* **50**, 1497–1499. https://doi.org/10.1039/C3CC48207C.

Hardin, W. G., Mefford, J. T., Slanac, D. A., Patel, B. B., Wang, X., Dai, S., Zhao, X., Ruoff, R. S., Johnston, K. P. & Stevenson, K. J. 2014 Tuning the electrocatalytic activity of perovskites through active site variation and support interactions. *Chem. Mat.* **26** (11), 2268–3376. https://doi.org/10.1021/cm403785q.

Hashemian, S. & Foroghimoqhadam, A. 2014 Effect of copper doping on $CoTiO_3$ ilmenite type nanoparticles for removal of congo red from aqueous solution. *Chem. Eng. J.* **235**, 299–306. http://dx.doi.org/10.1016/j.cej.2013.08.089.

Ho, Y. S. & Mckay, G. 1999 Pseudo-second order model for sorption processes. *Process Biochem.* **34**, 451–465.

Largitte, L. & Pasquier, R. 2016 A review of the kinetics adsorption models and their application to the adsorption of lead by an activated carbon. *Chem. Eng. Res. Des.* **109**, 495–504. http://dx.doi.org/10.1016/j.cherd.2016.02.006.

Lemos, J. A. S., Souza, V. M. S. C., Ribeiro, I. A., Souza, M. J. B. & Garrido Pedrosa, A. M. 2020 Study of the influence of perovskite structure site A metals on the adsorptive properties in liquid medium. In: *13 Brazilian Meeting on Adsorption*, online, 30 November–3 December.

Mahata, A., Datta, P. & Basu, R. N. 2017 Synthesis and characterization of Ca doped $lamno_3$ as potential anode material for solid oxide electrolysis cells. *Cer. Int.* **43**, 433–438. http://dx.doi.org/10.1016/j.ceramint.2016.09.177.

Mo, H., Nan, H., Lang, X., Liu, S., Qiao, L., Hu, X. & Tian, H. 2018 Influence of calcium doping on performance of $lamno_3$ supercapacitors. *Ceram. Int.* **44** (8), 9733–9741. https://doi.org/10.1016/j.ceramint.2018.02.205.

Muro, I. Z., Insausti, M., Lezama, L. & Rojo, T. 2005 Morphological and magnetic study of $CaMnO_{3-x}$ oxides obtained from diferente routes. *J. Sol. State Chem.* **178**, 928–936. https://doi.org/10.1016/j.jssc.2004.06.052.

Nascimento, E. V., Garrido Pedrosa, A. M. & Souza, M. J. B. 2020 The $LaMnO_3$ as adsorbent: kinetic studies and of the regeneration and reuse of adsorbent. In *13 Brazilian Meeting on Adsorption*, online, 30 November–3 December.

Oliveira, F. S., Pimentel, P. M., Oliveira, R. M. P. B., Melo, D. M. A. & Melo, M. A. F. 2010 Effect of lanthanum replacement by strontium in lanthanim nickelate crystal synthesized using gelatina as organic precursor. *Mater. Lett.* **64** (24), 2700–2703. https://doi.org/10.1016/j.matlet.2010.08.059.

Peña, M. A. & Fierro, J. L. G. 2001 Chemical strucutres and performance of perovskite oxides. *Chem. Rev.* **101** (7), 1981–2017. https://doi.org/10.1021/cr980129f.

Rakass, S., Hassani, H. O., Abboudi, M., Kooli, F., Mohmoud, A., Aljuhani, A. & Wadaani, F. A. 2018 Molybdenum Trioxide: efficient nanosorbent for removal of methylene blue dye from aqueous solution. *Molecules* **23** (9), 2295–2313. https://doi.org/10.3390/molecules23092295.

Ribeiro, J. F. S. 2019 *Estudo do Método de Síntese de Materiais com Estrutura Perovskita nas Características Estruturais E na Remoção do Corante Azul de Metileno (Study of the Synthesis Method of Materials with Perovskite Structure in the Structural Characteristics and in the Removal of the Methylene Blue dye)*. Master dissertation, Federal University of Sergipe, São Cristovão, Brazil.

Ribeiro, I. A., Couto, J. E., Lemos, J. A. S., Souza, M. J. B. & Garrido Pedrosa, A. M. 2020 Evaluation of red bezaktiv dye adsorption on the $LaCoO_3$ material. In: *13 Brazilian Meeting on Adsorption*, online, 30 November–3 December.

Rodrigues, P. A. S. 2016 *Quitosana como adsorvente para remoção de cor em solução aquosa de corante reativo (Chitosan as na Adsorbent for Color Removal in Aqueous Reactive dye Solution)*. Master dissertation, Federal University of Rio Grande do Norte, Natal, Brazil.

Sanaeishoar, T., Tavakkoli, H. & Mohave, F. 2014 A facile and eco-friendly synthesis of imidazo[1,2-a]pyridines using nano-sized $LaMnO_3$ perovskite-type oxide as an efficient catalyst under solvent-free conditions. *Appl. Catal. A-Gen.* **470**, 56–62. http://dx.doi.org/10.1016/j.apcata.2013.10.026.

Santos, A. G., Leite, J. O., Souza, M. J. B., Gimenez, I. F. & Garrido Pedrosa, A. M. 2018 Effect of the metal type in perovskites prepared by modified proteic method in dye adsorption from aqueous medium. *Ceram. Int.* **44**, 5743–5750. https://doi.org/10.1016/j.ceramint.2017.12.232.

Smiciklas, I. D., Milonic, S. K., Pfendt, P. & Raicevic, S. 2000 The point of zero charge and sorption of cadmium (II) and strontium (II) ions on synthetic hydroxyapatite. *Sep. Purif. Technol.* **18**, 185–194.

Souza, A. A. 2019 *Efeito do tipo de metal da estrutura perovsquita nas características estruturais e na utilização como adsorvente na remoção do corante vermelho congo (Effect of the Metal Type of the Perovskite Structure on Structural Characteristics and use as an Adsorbent in the Removal of Congo red dye)*. Master dissertation, Federal University of Sergipe, São Cristovão, Brazil.

Tabari, T., Singh, D., Calisan, A., Ebadi, M., Tavakkoli, H. & Caglar, B. 2017 Microwave assisted synthesis of $La_{1-x}Ca_xMnO_3$ $(x = 0, 0.2$ e $0.4)$: structural and capacitance properties. *Ceramics Int.* **43**, 15970–15977. http://dx.doi.org/10.1016/j.ceramint.2017.08.182.

Tanaka, H. & Misono, M. 2001 Advances in designing perovskite catalysts. *Curr. Opin. Solid State Mat. Sci.* **5**, 381–387.

Tavakkoli, H. & Moayedipour, T. 2014 Fabrication of perovskite-type oxide $La_{0,5}Pb_{0,5}MnO_3$ nanoparticles and its dye removal performance. *J. Nano Chem.* **4**, 115–124. https://doi.org/10.1007/s40097-014-0116-z.

Tavakkoli, H. & Yazdanbakhsh, M. 2013 Fabrication of two perovskite-type oxide nanoparticles as the new adsorbents in efficient removal of a pesticide from aqueous solutions:

kinetic, thermodynamic, and adsorptions studies. *Microporous Mesoporous Mat.* **176**, 86–94. http://dx.doi.org/10.1016/j.micromeso.2013.03.043.

Tavakkoli, H., Ghaemi, A. & Mostofizadeh, M. 2014 Synthesis and evaluation catalytic efficiency of perovskite-type oxide nanopowders in removal of bromocresol purple from aqueous solution. *Int. J. Sci.* **2** (7), 340–351.

Thommes, M., Kaneko, K., Neimark, A. V., Olivier, J. P., Rodriguez-Reinoso, F., Rouquerol, J. & Sing, K. S. W. 2015 Physisorption of gases, with special reference to the evaluation of surface area and pore size distribution (IUPAC Technical Report). *Pure Appl. Chem.* **87** (9–10), 1051–1069. https://doi.org/10.1515/pac-2014-1117.

Tummino, M. L., Laurenti, E., Deganello, F., Prevot, A. B. & Magnacca, G. 2017 Revisiting the catalytic activity of a doped $SrFeO_3$ for water pollutants removal: effect of light and temperature. *Appl. Catal. B-Environ.* **207**, 174–181. http://dx.doi.org/10.1016/j.apcatb.2017.02.007.

Vijayaraghavan, K., Padmesh, T. V. N., Palanivelu, K. & Velan, M. 2006 Biosorption of nickel (II) ions onto *Sargassum wightii*: application of two-parameter and three-parameter isotherm models. *J. Hazard. Mater.* **133** (1–3), 304–308. https://doi.org/10.1016/j.jhazmat.2005.10.016.

Walha, I., Ehrenberg, H., Fuess, H. & Cheikhrouhou, A. 2007 Structure and magnetic properties of lanthanum and calcium-deficient $La_{0,5}Ca_{0,5}MnO_3$ manganites. *J. All. Comp.* **433**, 63–67. https://doi.org/10.1016/j.jallcom.2006.06.095.

Yazdanbakhsh, M., Tavakkoli, H. & Hosseini, S. M. 2011 Characterization and evaluation catalytic efficiency of $La_{0,5}Ca_{0,5}NiO_3$ nanopowders in removal of reactive blue 5 from aqueous solution. *Desalination.* **281**, 388–395. https://doi.org/10.1016/j.desal.2011.08.020.

Zhu, J., Li, H., Zhong, L., Xiao, P., Xu, X., Yang, X., Zhao, Z. & Li, J. 2014 Perovskite oxides: preparation, characterization and applications in heterogeneous catalysis. *ACS Catal.* **4**, 2917–2940. https://doi.org/10.1021/cs500606 g.

First received 28 February 2021; accepted in revised form 21 April 2021. Available online 5 May 2021